Check for updates

Chemistry–A European Journal
Research Article
doi.org/10.1002/chem.202401218
Chemistry Europe
European Chemical Societies Publishing
www.chemeurj.org

Generation, Characterization and Reactivity of a High-Valent Mononuclear Cobalt(IV)–Diazide Complex

Michael Kayne,[a] Patrick S. Murphy,[b] Yubin M. Kwon,[a] Yuri Lee,[b] Timothy A. Jackson,*[b] and Dong Wang*[a]

High-valent Fe(IV)=O intermediates of metalloenzymes have inspired numerous efforts to generate synthetic analogs to mimic and understand their substrate oxidation reactivities. However, high-valent M(IV) complexes of late transition metals are rare. We have recently reported a novel Co(IV)–dinitrate complex (**1-NO$_3$**) that activates sp^3 C–H bonds up to 87 kcal/mol. In this work, we have shown that the nitrate ligands in **1-NO$_3$** can be replaced by azide, a more basic coordinating base, resulting in the formation of a more potent Co(IV)–diazide species (**1-N$_3$**) that reacts with substrates (hydrocarbons and phenols) at faster rate constants and activates stronger C–H bonds than the parent complex **1-NO$_3$**. We have characterized **1-N$_3$** employing a combination of spectroscopic and computational approaches. Our results clearly show that the coordination of azide leads to the modulation of the Co(IV) electronic structure and the Co(IV/III) redox potential. Together with the higher basicity of azide, these thermodynamic parameters contribute to the higher driving forces of **1-N$_3$** than **1-NO$_3$** for C–H bond activation. Our discoveries are thus insightful for designing more reactive bio-inspired high-valent late transition metal complexes for activating inert aliphatic hydrocarbons.

Introduction

High-valent Fe(IV)=O intermediates play critical roles in the catalytic cycles of many metalloenzymes and have inspired numerous efforts to generate synthetic analogs for better understanding their structural and electronic properties and substrate oxidation reactivities.[1] In a typical C–H bond activation reaction, an Fe(IV)=O moiety abstracts an H-atom from the substrate to generate an Fe(III)–OH species. In this process, the Fe(IV) center and the oxo ligand are the electron and proton acceptors, respectively. While M(IV)=O species of early and middle first-row transition metals have been extensively studied,[1a,2] high-valent complexes of late transition metals Co, Ni and Cu having a formal oxidation state of +4 are rare.[3] In particular, it is challenging to obtain stable M(IV)=O complexes of late transition metals as predicted by classical "oxo-wall" bonding theories.[4] Alternatively, diverging the synthetic efforts from the oxo to non-oxo (such as halide, hydroxide, acetate, and nitrate) ligands offers an applicable strategy to generate and investigate the corresponding M(IV)–X complexes.[5] Conceivably, the development of a series of M(IV)–X complexes with systematically modulated ligand X as the proton acceptor in an H-atom transfer (HAT) reaction can provide unprecedented insights into the substrate C–H bond activation reactivities of these M(IV) complexes.

Recently, we have reported the generation, characterization and C–H bond activation reactivity of a mononuclear Co(IV)–$(ONO_2)_2$ complex (**1-NO$_3$**, Scheme 1) supported by a tridentate, dianionic N3 ligand L (L=2,6-bis((2-(2,6-dimethylphenylamino))isopropyl)pyridine).[3e] **1-NO$_3$** is a square pyramidal complex with two nitrate ligands coordinating in two different environments, showing a long axial Co–ONO_2 bond at 2.100 Å and a short one at 1.927 Å on the equatorial position. Characterization of **1-NO$_3$** by EPR spectroscopy and DFT calculations clearly shows that the unpaired electronic spin is predominantly located on the Co(IV) d_{z2} molecular orbital (MO). **1-NO$_3$** is able to cleave sp^3 C–H bonds as strong as those in ethylbenzene (87 kcal/mol) and we have proposed that the

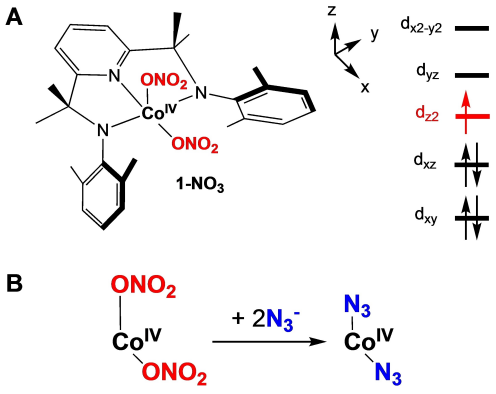

Scheme 1. (A) Schematic structure of **1-NO$_3$** and its *d*-orbital splitting pattern. (B) Ligand substitution reaction to generate **1-N$_3$** in this work.

[a] M. Kayne, Dr. Y. M. Kwon, Prof. Dr. D. Wang
Department of Chemistry and Biochemistry, Center for Biomolecular Structure and Dynamics
University of Montana
Missoula, Montana 59812, United States
E-mail: dong1.wang@umontana.edu

[b] P. S. Murphy, Dr. Y. Lee, Prof. Dr. T. A. Jackson
Department of Chemistry and Center for Environmentally Beneficial Catalysis
University of Kansas
Lawrence, Kansas 66045, United States
E-mail: taj@ku.edu

Supporting information for this article is available on the WWW under https://doi.org/10.1002/chem.202401218

© 2024 Wiley-VCH GmbH

Co(IV) d_{z2} MO and the axial nitrate ligand act as the electron and proton acceptors, respectively, in a HAT reaction.

The effects of coordinating anions on the C–H bond activation reactivity of mononuclear and dinuclear high-valent metal–oxo complexes have been investigated and documented by a number of groups, including us, for a variety of systems.[6] In most cases, the coordination of a Lewis base modulates the geometric and electronic properties of the metal–oxo species, and subsequently tunes the electron affinity (redox potential) of the metal center (electron acceptor) and the proton affinity (pK_a) of the oxo group (proton acceptor) in a C–H bond activation reaction. By contrast, our Co(IV) complex **1-NO$_3$** lacks the oxo moiety and alternatively utilizes the axial nitrate ligand as the proton acceptor in a HAT reaction. Therefore, we hypothesize that the introduction of a stronger base X will replace the proton accepting nitrate ligand in **1-NO$_3$**, which will likely increase the interaction of this ligand with the Co(IV) center and subsequently destabilize the Co(IV) d_{z2} MO. The modification of the Co(IV) electronic structure and the employment of a stronger base as the proton accepting ligand will likely modulate the substrate C–H bond activation reactivity.

In this work, we have tested this hypothesis by generating and characterizing a novel Co(IV)–diazide complex (**1-N$_3$**) using azide (a stronger base than nitrate) anions to replace the nitrate ligands of **1-NO$_3$** (Scheme 1). As expected, **1-N$_3$** exhibits a stronger ligand–metal interaction on the axial position than **1-NO$_3$**, which perturbs the *d*-orbital splitting pattern and the electronic structure of the Co(IV) center and in turn leads to the changes of the spectroscopic properties. Interestingly, **1-N$_3$** exhibits higher oxidative reactivities than **1-NO$_3$** with substrate C–H and O–H bonds both thermodynamically and kinetically. The measurements of the Co(IV/III) redox potentials further reveal that **1-N$_3$** is 0.43 V more oxidizing than **1-NO$_3$**. Together with that azide is a stronger base than nitrate, these results demonstrate than **1-N$_3$** has electron and proton affinities that are both higher than those of **1-NO$_3$** and should be a more potent HAT reagent. Our work has thus provided valuable insights into further tuning the cobalt system for activating more inert aliphatic C–H bonds.

Results and Discussion

1. Generation and characterization of the Co(IV)–$(N_3)_2$ complex. The starting complex Co(IV)–$(ONO_2)_2$ (**1-NO$_3$**) can be obtained in a high yield of >90% following a synthetic procedure we have reported recently.[3e] Complex **1-NO$_3$** is stable at room temperature for a few hours. However, the introduction of 3 eq. tetrabutylammonium azide ($TBAN_3$) into the acetonitrile solution of **1-NO$_3$** causes its decay within 30 min (Figure 1). This observation suggests that the interaction of **1-NO$_3$** with azide results in an accelerated reduction of the Co(IV) center. A close examination of the spectral changes for this self-decay reaction indicates that a short-lived intermediate is formed within 2 seconds after the addition of the azide salt. We attribute this process to rapid exchange of the nitrate ligand(s) in **1-NO$_3$** by azide to form a Co(IV)–azide complex (**1-N$_3$**, Figure 1 blue trace), which is followed by first-order decay of **1-N$_3$** to generate a Co(III) product complex at 584 nm, affording a first-order rate constant $k_1 = 0.002\ s^{-1}$ (Figure 1, inset). Two isosbestic points are observed at 509 nm and 660 nm in the course of transformation from **1-N$_3$** to Co(III), suggesting that no other intermediate is involved in this process.

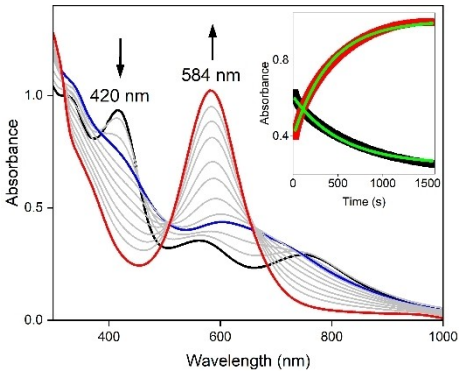

Figure 1. Spectral changes showing the self-decay of 0.1 mM **1-NO$_3$** (black) first to an intermediate (blue) and then to a Co(III) species (red) in the presence of 3 eq. $TBAN_3$ in acetonitrile at room temperature. Inset: time traces for the conversion of the blue spectrum to the red spectrum monitored at 420 nm (black) and 584 nm (red), best fitted using a first-order exponential model (green curves).

Because of the transient nature of **1-N$_3$** at room temperature, we have carried out additional experiments at cryogenic temperatures in order to stabilize this complex for characterization. Indeed, the addition of 3 eq. $TBAN_3$ to the acetonitrile solution of **1-NO$_3$** at −40 °C causes the rapid conversion of **1-NO$_3$** to a new green chromophore at 650 nm (Figure 2A). A titration experiment shows that 2 eq. azide is necessary to fully generate **1-N$_3$** (Figure 2A inset), indicating that both nitrate ligands in complex **1-NO$_3$** are replaced by azide. Once **1-N$_3$** is formed, adding an excess amount of $TBANO_3$ does not convert it back to **1-NO$_3$**, consistent with azide as a stronger base than nitrate. **1-N$_3$** is stable only at −40 °C for a few hours and converts back to Co(III) upon warming to room temperature (Figure S1), suggesting that **1-N$_3$** is a more reactive species than **1-NO$_3$**.

We have been able to crystalize **1-N$_3$** and have its structure solved by X-ray crystallography. As shown in Figure 2B, **1-N$_3$** is a five-coordinated Co(IV)–$(N_3)_2$ complex with two azide anions replacing both nitrate ligands of **1-NO$_3$**, consistent with the results obtained from titration experiments. Very interestingly, the axial Co–N_3 bond (1.937 Å) in **1-N$_3$** is significantly shorter than the corresponding Co–ONO_2 distance (2.100 Å) in **1-NO$_3$** (Table 1), clearly revealing a stronger interaction of Co(IV) with azide than with nitrate on the axial position. In the equatorial position, the Co–X and Co–N(ligand) distances for the two complexes are almost identical. Furthermore, the Co(IV)–azide distances in **1-N$_3$** are shorter than those in a number of Co(III)–$(N_3)_2$ and Fe(III)–$(N_3)_2$ complexes reported previously.[7] This observation shows that the azide ligands interact more strongly with high-valent Co(IV) than Co(III) and Fe(III), both having lower oxidation states.

© 2024 Wiley-VCH GmbH

15213765, 2024, 35, Downloaded from https://chemistry-europe.onlinelibrary.wiley.com/doi/10.1002/chem.202401218 by University Of Kansas, Wiley Online Library on [22/07/2024]. See the Terms and Conditions (https://onlinelibrary.wiley.com/terms-and-conditions) on Wiley Online Library for rules of use; OA articles are governed by the applicable Creative Commons License

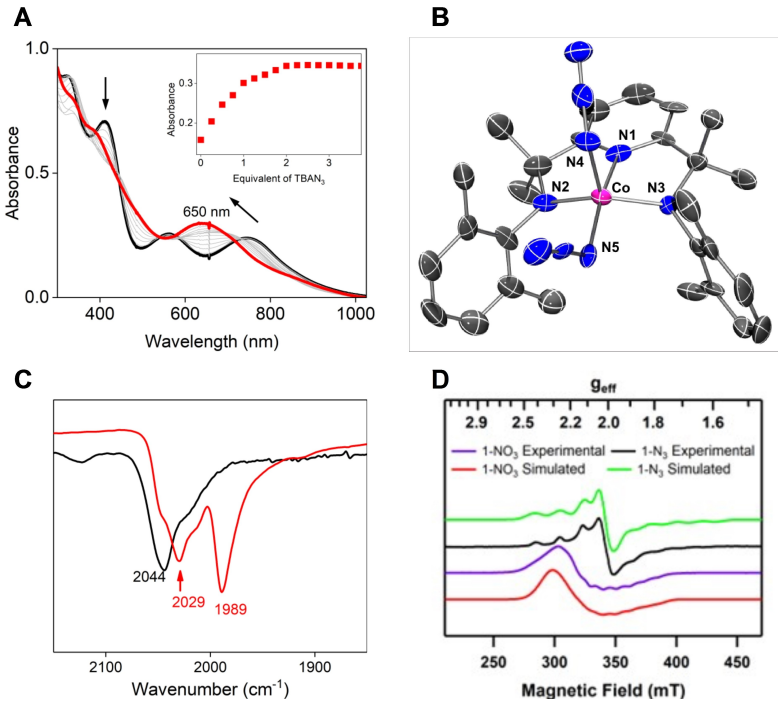

Figure 2. (A) Titration of 0.1 mM **1-NO$_3$** with TBAN$_3$ in acetonitrile at −40 °C, showing spectral changes from **1-NO$_3$** (black) to **1-N$_3$** (red). Inset: titration curve monitored at 650 nm showing that 2 eq. azide is needed to fully generate **1-N$_3$**. (B) Crystal structures of **1-N$_3$**, selected bond lengths and angle: Co–N1, 1.871 Å; Co–N2, 1.830 Å; Co–N3, 1.835 Å; Co–N4, 1.934 Å; Co–N5, 1.925 Å; N4–Co–N5, 94.1°. Thermal ellipsoids are drawn at the 50% probability level. Hydrogen atoms are ignored for clarity. (C) Solid state FTIR spectra of Co(III)–N$_3$ (black) and **1-N$_3$** (red). (D) Perpendicular-mode X-band EPR spectra of **1-N$_3$** (black) and **1-NO$_3$** (purple) and simulations (green and red, respectively) in MeCN at 10 K. Sample concentrations are 5 mM.

Table 1. Bond lengths (Å) and angles (degrees) from crystal and DFT structures of Co(IV) complexes.

Complex	N1	N2	N3	X (axial)[a]	X (equatorial)[a]	X–Co–X[b]	N1–Co–X$_{eq}$[c]	N2–Co–N3
1-NO$_3$ (XRD)	1.863	1.831	1.834	2.100	1.927	82.0	178.3	154.7
1-NO$_3$ (DFT)	1.864	1.832	1.826	2.083	1.936	79.6	179.7	153.0
1-N$_3$ (XRD)	1.871	1.830	1.835	1.937	1.925	94.1	169.1	149.5
1-N$_3$ (DFT)	1.869	1.844	1.844	1.914	1.955	93.8	170.0	150.0

[a]X = N$_3$ or NO$_3$. [b]Bond angle between axial and equatorial X ligands. [c]Bond angle between N1 and axial X ligand.

The solid state FTIR spectrum of **1-N$_3$** (Figure 2C) clearly shows two signals at 2029 cm^{-1} and 1989 cm^{-1} assignable to the asymmetric intra-azide stretching mode ($\upsilon_{as}(N_3^-)$),[7] indicating that the two azide ligands are located in two different environments. By contrast, the spectrum of the corresponding Co(III)–N$_3$ derivative shows only one vibrational band at 2044 cm^{-1}. These data compare favorably with those of related cobalt and iron–azide complexes reported by other groups in previous work.[7] The $\upsilon_{as}(N_3^-)$ values for this group of complexes fall into a typical range of 2010–2070 cm^{-1}. Complexes with two azide ligands in a *cis*-configuration all show two different vibrations; while the one with two azide ligands in a *trans*-configuration exhibits only one $\upsilon_{as}(N_3^-)$ value. Therefore, our observation of two stretching frequencies for **1-N$_3$** is indicative of the *cis*-configuration for the two azide ligands. These results are also consistent with the crystal structures of **1-N$_3$** and Co(III)–N$_3$ (Figures 2B and Figure S2), showing two inequivalent and only one azide ligand(s), respectively. To aid in assigning the IR vibrations, numerical frequency calculations were run for both **1-N$_3$** and Co(III)–N$_3$. For **1-N$_3$**, two antisymmetric stretching frequencies at 2030 cm^{-1} and 2061 cm^{-1} are predicted for the axial and equatorial azide ligands, respectively. For Co(III)–N$_3$ the antisymmetric stretch for the equatorial azide is calculated at 2067 cm^{-1}. These computations reproduce the experimental results well, with only a ~30 cm^{-1} difference observed between the experimental and calculated azide vibrations.

The perpendicular-mode, X-band EPR spectrum of **1-N$_3$** collected at 10 K shows a prominent derivative signal centered near $g = 2.0$ that contains hyperfine features at lower and higher fields (Figures 2D and S3). These hyperfine signals are attributed to the ^{59}Co ($I = 7/2$) nucleus. The average splitting between the hyperfine signals reveals an $A \approx 17$ mT (~500 MHz). The EPR spectrum of **1-N$_3$** can be well simulated as an axial signal with $g_1 = g_2 = 2.02$, $g_3 = 1.93$ and $A_1 = A_2 = 1.6$ mT, and $A_3 = 20.3$ mT. Attempts to fit the spectrum assuming a rhombic g matrix were not successful. The large value for A_3 is required

© 2024 Wiley-VCH GmbH

15213765, 2024, 35, Downloaded from https://chemistry-europe.onlinelibrary.wiley.com/doi/10.1002/chem.202401218 by University Of Kansas, Wiley Online Library on [22/07/2024]. See the Terms and Conditions (https://onlinelibrary.wiley.com/terms-and-conditions) on Wiley Online Library for rules of use; OA articles are governed by the applicable Creative Commons License

to reproduce the eight hyperfine signals that flank the central derivative. This large hyperfine value is suggestive of strong coupling between the unpaired electron and the ^{59}Co nucleus, which would imply that the SOMO carries a high degree of Co 3d character. The band shape of the EPR spectrum of **1-N$_3$** is distinct from that of the previously reported analogue containing nitrate ligands (**1-NO$_3$**).[3e] The previously reported EPR spectrum for **1-NO$_3$**, which is included in Figure 2D for comparison, shows a broad, derivative-shaped signal that spans 270–400 mT, with a crossing point at $g = 2.2$ (320 mT). ^{59}Co hyperfine features are observed on the negative component of the derivative. As described previously, this spectrum has been simulated as a slightly rhombic system with $g = 2.23$, 2.08, and 2.00, and $A = 4.38$, 5.35, and 10.4 mT (although the unusual breadth of this EPR signal creates some uncertainty in the EPR parameters used in the simulation). The differences between the EPR spectra of **1-N$_3$** and **1-NO$_3$** suggest important changes in the ground state electronic structures of these complexes. As discussed below, electronic structure computations reveal that these differences can be linked to a change in the SOMO of **1-N$_3$** compared to **1-NO$_3$**.

The EPR parameters for **1-N$_3$** fall within the range of those reported for $S = 1/2$ Co(IV) centers ($g \approx 2.14$–1.89 and $A \approx 9.5$–2 mT).[8] An alkylcobalt(IV) species with a salen ligand also showed an axial EPR spectrum, but with a larger shift in one g value ($g_{\parallel} = 2.178$ and $g_{\perp} \approx 2$) and a ^{59}Co hyperfine tensor with $A_{\parallel} = 8.5$ mT and $A_{\perp} \approx 3$ mT.[8d] In that case, the larger deviation of $g_{\parallel}$ from 2.0 and the large $A_{\parallel}$ value were taken as evidence of a high degree of spin density on the Co(IV) center (calculated as $+0.85$ e$^-$ using DFT computations).[8d] An axial spectrum was also recently reported for a Co(IV)–imido complex with a tripodal supporting ligand ($g_{\parallel} = 2.12$ and $g_{\perp} \approx 2.09$, with ^{59}Co hyperfine of $A_{\parallel} = 9.5$ mT and $A_{\perp} \approx 5.32$ mT (reported as $A_{\parallel} = 96.3\times10^{-4}$ cm^{-1} and $A_{\perp} \approx 49.7\times10^{-4}$ cm^{-1}).[8e] In terms of overall appearance, the EPR spectrum of **1-N$_3$** is quite similar to that reported for a five coordinate, formally Co(IV) center with equatorial dithiolene ligands and an axial phosphine ligand.[8c] That spectrum also consisted of a central derivative peak flanked by hyperfine signals. However, for the Co–dithiolene complex, the EPR signals spanned the narrow field range of ~315–355 mT, which stands in contrast to the broader field distribution for the signals of **1-N$_3$** (~280–410 mT). As noted above, the broader field distribution of the EPR signals of **1-N$_3$**, which is reflected in the large A_3 parameter, provides good support for a high degree of spin density at the Co center.

2. Computational studies of the Co(IV)–(N$_3$)$_2$ complex. We have used DFT computations to optimize a structure for **1-N$_3$** (Figure 3), which permits a comparison of a DFT computed structure with that determined by X-ray crystallography. The Co–N bond lengths in the DFT structure are in excellent agreement with the corresponding lengths in the crystal structure (Table 1). For example, the calculated Co–N bonds involving the pincer ligand are all near 1.84 Å, with the Co–N(pyridine) distance (1.869 Å) longer than the Co–N(amido) distances (1.844 Å). The bonds to the azide ligands are both above 1.91 Å, and the N4–Co–N5 angle is also in excellent agreement with the X-ray structure. We had previously used this same DFT method to develop a structure for **1-NO$_3$** and also observed good agreement between the DFT and X-ray structures (Table 1).[3e]

We have then employed DFT and CASSCF computations to probe the electronic structure of **1-N$_3$**. Using a coordinate system where the z axis lies along the axial Co–N$_3$ bond and the equatorial Co–N bonds are roughly along the x and y axes, the Co 3d$_{z2}$ and 3d$_{x2-y2}$ MOs are (predominantly) σ-type orbitals. Surface contour plots for these MOs reveal large ligand characters (see Figure 3 for the 3d$_{z2}$ MOs). In particular, the 3d$_{x2-y2}$ MO has large contributions from the amido (8.4%), pyridine (6.4%), and equatorial azide (11.0%) donors, while the 3d$_{z2}$ MO shows strong σ-antibonding character with the axial azide ligand (19.7%) and π-antibonding character with the amido donors (13.3%, MO compositions are given in Table S1). The π-character in the Co 3d$_{z2}$ MO is caused by the distortion of the Co atom above the ligand plane, as reflected in the N2–Co–N3 angle of 150° (Table 1). The strong interactions between the ligands and the Co 3d$_{x2-y2}$ and 3d$_{z2}$ MOs place these orbitals at relatively high energy, and each of these MOs is unoccupied (Figure 3, left).

Slightly beneath the Co 3d$_{x2-y2}$ and 3d$_{z2}$ MOs of **1-N$_3$** are the Co 3d$_{yz}$, 3d$_{xy}$, and 3d$_{xz}$ MOs (Figure 3, left). These latter MOs are involved in π-interactions with the ligands, and their relative ordering reflects the strengths of the different π-donors. Among

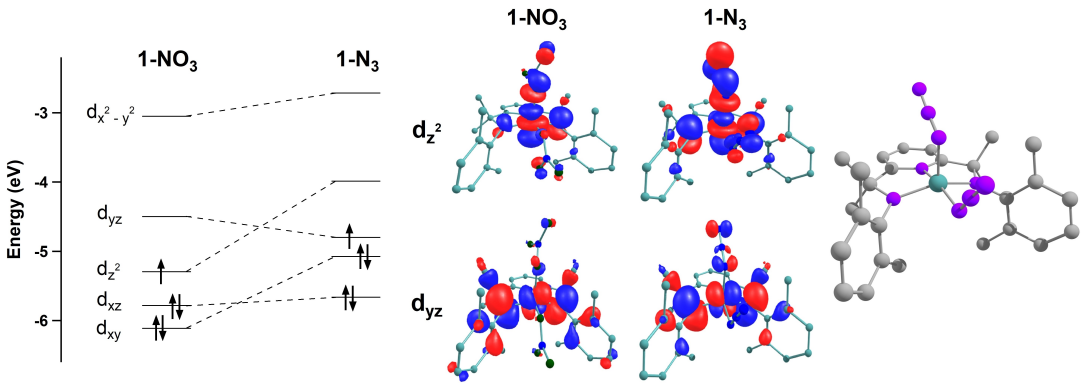

Figure 3. Left: DFT energy level diagram from Co 3d-based MOs of **1-X** complexes. Energies are for the α-spin Kohn-Sham orbitals. Center: DFT surface contour plots of the d$_{yz}$ and d$_{z2}$ quasi-restricted orbitals for **1-X** complexes. Right: DFT optimized geometry for **1-N$_3$**.

© 2024 Wiley-VCH GmbH

15213765, 2024, 35, Downloaded from https://chemistry-europe.onlinelibrary.wiley.com/doi/10.1002/chem.202401218 by University Of Kansas, Wiley Online Library on [22/07/2024]. See the Terms and Conditions (https://onlinelibrary.wiley.com/terms-and-conditions) on Wiley Online Library for rules of use; OA articles are governed by the applicable Creative Commons License

this set of MOs, the Co $3d_{yz}$ MO is at highest energy and, consequently, is the singly occupied MO for **1-N_3** (Figure 3, left). This MO has strong π-antibonding interactions with the amido donors (34.6%) and carries some π-antibonding character with the axial azide ligand (6.8%) as well. The Co $3d_{xy}$ and $3d_{xz}$ MOs are at slightly lower energy and each of these MOs is doubly occupied. These MOs have π-antibonding interactions with the equatorial and axial azide ligands, respectively. Overall, the DFT computations predict a $(3d_{xz})^2(3d_{xy})^2(3d_{yz})^1(3d_{z2})^0(3d_{x2\text{-}y2})^0$ configuration, consistent with an $S=1/2$ Co(IV) center, albeit with highly covalent Co 3d-based MOs.

As a complement to the DFT computations, we have also explored the electronic structure of **1-N_3** using CASSCF/NEVPT2 computations. The CASSCF/NEVPT2 calculation using a CAS(13,9) active space yields a doublet ($S=1/2$) ground state, consistent with experiments. This ground state is highly multiconfigurational, with contributions from states with different occupancies of metal-based and ligand-based orbitals. Surface contour plots for these orbitals are in Figure S4. These orbitals are labeled according to their leading contributions from the Co 3d manifold, the axial or equatorial azide ligands (N_3^{ax} or N_3^{eq}, respectively), or the pincer ligand (L). The leading configurations (Table S2) are as follows:

$(N_3^{ax}\text{-}d_{z2})^2(L\text{-}d_{yz})^2(L\text{-}d_{x2-y2})^2(d_{z2}\text{-}N_3^{eq})^1(d_{yz})^1(N_3^{eq}\text{-}d_{z2})^1(d_{x2-y2})^0$ (configuration 1; 20%)

$(N_3^{ax}\text{-}d_{z2})^2(L\text{-}d_{yz})^2(L\text{-}d_{x2-y2})^2(d_{z2}\text{-}N_3^{eq})^0(d_{yz})^1(N_3^{eq}\text{-}d_{z2})^2(d_{x2-y2})^0$ (configuration 2; 15%)

$(N_3^{ax}\text{-}d_{z2})^1(L\text{-}d_{yz})^2(L\text{-}d_{x2-y2})^2(d_{z2}\text{-}N_3^{eq})^2(d_{yz})^1(N_3^{eq}\text{-}d_{z2})^1(d_{x2-y2})^0$ (configuration 3; 10%)

$(N_3^{ax}\text{-}d_{z2})^1(L\text{-}d_{yz})^2(L\text{-}d_{x2-y2})^2(d_{z2}\text{-}N_3^{eq})^1(d_{yz})^1(N_3^{eq}\text{-}d_{z2})^2(d_{x2-y2})^0$ (configuration 4; 9%)

$(N_3^{ax}\text{-}d_{z2})^2(L\text{-}d_{yz})^2(L\text{-}d_{x2-y2})^2(d_{z2}\text{-}N_3^{eq})^2(d_{yz})^1(N_3^{eq}\text{-}d_{z2})^0(d_{x2-y2})^0$ (configuration 5; 7%)

These distinct configurations arise from different occupancies of highly covalent orbitals of mixed Co $3d_{z2}$ and N_3^- character. Configurations 3 and 4, in particular, are best interpreted as charge-transfer configurations, suggesting partial azide hole character. In support, a plot of the spin density for **1-N_3** from the CASSCF computations (Figure S5) shows negative spin density on the equatorial azide ligand. This non-negligible hole character suggests that the Co(IV) assignment should be viewed as a formal description. In each CASSCF configuration, the Co $3d_{yz}$ MO is singly occupied, which complements the DFT results where the Co(IV) d_{yz} MO is the SOMO. The g values calculated for the CASSCF/NEVPT2 ground state ($g=2.06$, 1.99, and 1.86, Table S3) are in reasonable agreement with the values obtained from EPR simulations ($g=2.02$, 2.02, and 1.93). The calculated ^{59}Co hyperfine parameters ($|A|=2.28$, 3.86, and 12.4 mT) reasonably reproduce the values of A from the simulation of the experimental EPR spectrum ($A=1.61$, 1.61, and 20.3 mT).

A comparison of the frontier MOs for **1-N_3** and **1-NO_3** reveals significant perturbations in MO energies caused by the coordinating anion. Most importantly, there is a change in the SOMO from **1-N_3** to the previously reported **1-NO_3** complex (Figure 3, left). In **1-N_3**, the strong interaction between the Co(IV) center and the axial azide ligand destabilizes the Co $3d_{z2}$ MO, causing it to lie above the $3d_{yz}$ SOMO. In contrast, the interaction of the Co(IV) center of **1-NO_3** with the axial nitrate ligand is relatively weak, as exemplified by the long axial Co–ONO_2 distance of 2.100 Å (Table 1). This weaker interaction leads the Co $3d_{z2}$ MO to lie below the Co $3d_{yz}$ MO, giving a Co $3d_{z2}$ SOMO for **1-NO_3**. Thus, the strength of the interaction of the Co center with the axial ligand (N_3^- or NO_3^-) controls the ordering the $3d_{yz}$ or $3d_{z2}$ MOs and, consequently, dictates the character of the SOMO ($3d_{yz}$ or $3d_{z2}$). We suggest that this difference in SOMO can account for the different EPR signals for **1-N_3** and **1-NO_3**. In support, CASSCF/NEVPT2 calculations for these two complexes, which reproduce the difference in SOMO character observed in the DFT calculations, yield quite distinct g and A values (Table S3).

3. Substrate oxidations. The self-decay profile of **1-N_3** clearly shows that it is a more reactive species than **1-NO_3**. We are thus interested in investigating its HAT reactions with substrates such as hydrocarbons and phenols. We have previously reported C–H bond activation reactivities of **1-NO_3** at room temperature. Therefore, we decided to carry out the studies of **1-N_3** at the same reaction temperature so that the results can be closely compared between these two Co(IV) complexes. As shown in Figure 1, the rapid generation of **1-N_3** within 2 seconds at room temperature ensures that the rest of the kinetics truly represents its reaction with a substrate.

3.1. C–H bond oxidations. We first employ 9,10-dihydroanthracene (DHA) as a probe substrate. **1-N_3** reacts with DHA to afford a second-order rate constant (k_2) of 0.58 $M^{-1}s^{-1}$ (Figures 4A and 4B), which is approximately one order of magnitude higher than that of **1-NO_3** (0.079 $M^{-1}s^{-1}$). The DHA oxidation rate is independent of the amount of azide added in a range of 2–5 eq. A H/D kinetic isotope effect (KIE) of 2.9 is determined when DHA is replaced by DHA-d_4 as the substrate (Figure 4B), suggesting that the cleavage of the substrate C–H bond is the rate-determining step for the reaction. The cobalt product after the reaction exhibits a strong absorbance at 584 nm indicative of the formation of Co(III) complex (Figure S1).[9] The DHA oxidation product is analyzed and quantified using GC-MS, showing the formation of anthracene in ~45% yield. Therefore, the Co(IV) complex is still a one-electron oxidant in the presence of azide. Adding more CAN into the post-reaction solution results in the re-oxidation of Co(III) to Co(IV), followed by converting Co(IV) back to Co(III) by the substrate (Figure S6). Such a cycle can be repeated multiple times. At the end of each cycle, ~85–90% of Co(III) is recovered after dilutions of the sample solution are taken into account. We interpret this result to indicate that the ligand is robust, even in these reactions that generate protons, suggesting that the N3 ligand is not protonated during the reaction. We have further carried out a control experiment using 2,6-di-*tert*-butylpyridine (pK_a(MeCN) = 15.2) and found that the DHA oxidation rate by **1-NO_3** in the

© 2024 Wiley-VCH GmbH

15213765, 2024, 35, Downloaded from https://chemistry-europe.onlinelibrary.wiley.com/doi/10.1002/chem.202401218 by University Of Kansas, Wiley Online Library on [22/07/2024]. See the Terms and Conditions (https://onlinelibrary.wiley.com/terms-and-conditions) on Wiley Online Library for rules of use; OA articles are governed by the applicable Creative Commons License

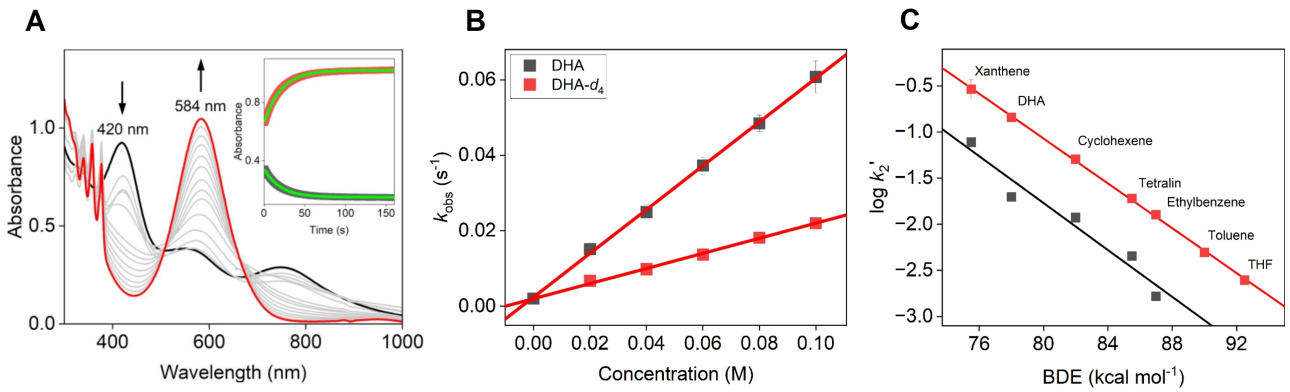

Figure 4. (A) Spectral changes showing the reaction of 0.1 mM **1-NO$_3$** (black) with 100 mM DHA in the presence of 3 eq. TBAN$_3$ in acetonitrile at room temperature. Inset: time traces monitored at 420 nm (black) and 584 nm (red), best fitted using a first-order exponential model (green curves). (B) Plots of k_{obs} as a function of the concentration of DHA (black) and DHA-d_4 (red) for their reactions with **1-NO$_3$** in the presence of 3 eq. TBAN$_3$, fitted linearly. (C) Plots of log k_2′ vs. the C–H bond strength for substrate oxidations by **1-NO$_3$** (black) and **1-N$_3$** (red). The lines represent the best linear fits with slopes of −0.13 (black) and −0.12 (red) (kcal mol^{-1})$^{-1}$.

presence of 3 eq. of this non-coordinating base is only 0.10 M^{-1} s^{-1} (less than two-fold difference compared to that of **1-NO$_3$** itself). Therefore, the rate enhancement for DHA oxidation observed with the addition of azide cannot be attributed to the accelerated proton transfer by the external Lewis base in a multiple-site concerted proton-electron transfer (MS-CPET) process,[9] and is consistent with a direct interaction between azide and the Co(IV) center.

The rate enhancements are also observed for a variety of hydrocarbon substrates in a broad range of the C–H bond strengths (Figures S7–S12, Table S4). As clearly shown in Figure 4C, the logarithm of the normalized rate constant (log k_2′) on a per hydrogen basis correlates linearly as a function of the substrate C–H bond strength for both **1-N$_3$** and **1-NO$_3$**. **1-N$_3$** reacts with all substrates studied about one order of magnitude faster than **1-NO$_3$**. The two correlations have almost identical slopes of approximately −0.12 (kcal mol^{-1})$^{-1}$, indicating that the active oxidants in these systems have similar sensitivity to the C–H bond strength of the substrates. Another notable observation is that the presence of azide not only increases the kinetic rate constants, but also results in the activation of stronger C–H bonds. For example, complex **1-NO$_3$** is only able to cleave C–H bonds up to 87 kcal/mol as those in ethylbenzene.[3e] This thermodynamic limit can be pushed to 92 kcal/mol as those in THF for **1-N$_3$** (Figure 4C). For all substrates studied, H/D KIEs in the typical range of 1.9–9.4 are obtained (Table S4). Oxygenated product(s) such as alcohol, aldehyde and ketone are formed in these reactions, presumably because the substrate radical is trapped by O_2 present in the reaction media after the C–H bond is cleaved. No azidation or other functionalized product(s) are identified. Taken together, it is apparent that the azide as a Lewis base enhances the C–H bond activation reactivity of Co(IV) both thermodynamically and kinetically without changing its nature as a one-electron oxidant.

3.2. O–H bond oxidations. We have then sought to investigate in a greater depth the HAT reactions of both Co(IV) complexes using phenol and derivatives as the H-atom donating substrates. As shown in Figure S13, **1-NO$_3$** reacts with phenol to afford a k_2 of 3.5 M^{-1} s^{-1}. A H/D KIE of 1.3 is determined using deuterated phenol as the substrate indicative of a HAT reaction. On the other hand, **1-N$_3$** is about one order of magnitude more reactive than **1-NO$_3$**, affording k_2 = 51 M^{-1} s^{-1} and a H/D KIE of 1.8 (Figure S14).

The employment of phenol derivatives with electron-donating or electron-withdrawing *para*-substituents further reveals more mechanistic details. For both complexes, the substrates with electron-donating groups react faster than those having electron-withdrawing groups (Table S5). The Hammett plots (Figure 5A) show that the value of log k_2 correlates linearly with the Hammett parameter σ_p, affording slopes $\rho = -1.00$ for **1-NO$_3$** and $\rho = -1.20$ for **1-N$_3$** consistent with the electrophilic nature for both Co(IV) complexes. Moreover, the Marcus plots of (RT/F)ln k_2 vs. the phenol oxidation potential E_{ox} (Figure 5B) exhibit also two linear correlations with slopes of −0.07 and −0.09 for **1-NO$_3$** and **1-N$_3$**, respectively. These near-zero slopes, along with the H/D KIE values, strongly indicate that for both complexes the phenol oxidations proceed through a HAT mechanism.[5b,10] Lastly, the plots of log k_2 as a function of the phenol O–H bond dissociation free energy (BDFE, Figure 5C) show two linear correlations with slopes of −0.12 and −0.16 (kcal mol^{-1})$^{-1}$ for **1-NO$_3$** and **1-N$_3$**, respectively. Interestingly, these slopes are highly similar to those obtained for C–H bond oxidations by these two Co(IV) species (−0.13 for **1-NO$_3$** and −0.12 for **1-N$_3$**, Figure 4C), indicating that both complexes have similar sensitivities to the strength of the C–H/O–H bond to be cleaved in HAT reactions.

3.3. Thermodynamic considerations. Based on the Bordwell-Polanyi relationship that has been applied to numerous cases,[11] the ability of a metal–oxo complex, represented by the strength of the O–H bond formed (D(O–H)), to abstract an H-atom includes two individual components: the electron affinity as indicated by the redox potential (E) of the $M^{(n+1)+/n+}$ couple and the proton affinity expressed as the pK_a of the oxo ligand (eq. 1).

© 2024 Wiley-VCH GmbH

15213765, 2024, 35, Downloaded from https://chemistry-europe.onlinelibrary.wiley.com/doi/10.1002/chem.202401218 by University Of Kansas, Wiley Online Library on [22/07/2024]. See the Terms and Conditions (https://onlinelibrary.wiley.com/terms-and-conditions) on Wiley Online Library for rules of use; OA articles are governed by the applicable Creative Commons License

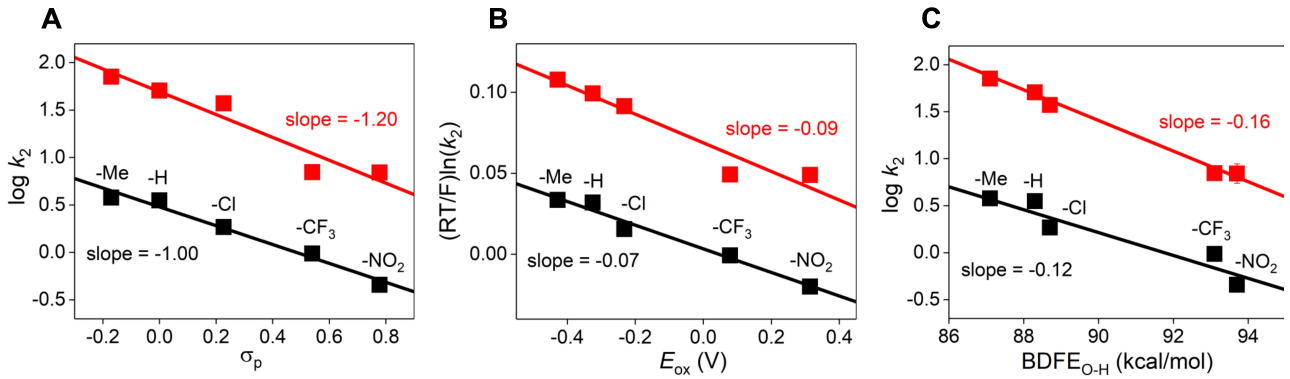

Figure 5. (A) Hammett correlation, (B) Marcus plot of (RT/F)lnk_2 vs. $E_{ox}(^{X}PhO^{\bullet}/^{X}PhOH)$, and (C) BDE plot of logk_2 vs. the phenol O–H bond strength for the reaction of **1-NO$_3$** (black) and **1-N$_3$** (red) with *para*-X-substituted phenol derivatives.

$$D_{O-H} = 23.06E(M^{(n+1)+/n+}) + 1.37pK_a + C \quad (1)$$

For non-oxo complexes that utilize other anionic ligands as the proton acceptor in HAT reactions, the pK_a of the proton accepting ligand represents the proton affinity. However, a non-oxo, anionic ligand likely dissociates from the metal center when protonated, making it challenging to accurately determine its pK_a while it is still bound to the metal. Alternatively, the pK_a of the free anion could be considered as an upper limit of the proton affinity since the coordination of the anionic ligand to a metal center will make it less basic. In our recent work,[3e] we have applied this method to estimate the upper bound of $D(Co^{III}(O–H)NO_2) = 84$ kcal/mol for complex **1-NO$_3$** using the measured Co(IV/III) redox potential of 0.55 V vs. ferrocene and the pK_a of free nitric acid (8.8) in acetonitrile.[12] This result provides a gratifying explanation for the ability of **1-NO$_3$** to cleave C–H bonds up to 87 kcal/mol.

In the present work, we first use cyclic voltammetry (CV) to measure the Co(IV/III) redox potential of **1-N$_3$**. These experiments are carried out using Co(III)–N_3 as the starting complex (Figure S1) in the presence of 5 eq. $TBAN_3$ to provide the additional azide needed to generate **1-N$_3$**. As shown in Figure 6, the CV of Co(III)–N_3 at room temperature shows an anodic peak at $E_{p,a} = 1.02$ V vs. ferrocene corresponding to the oxidation of

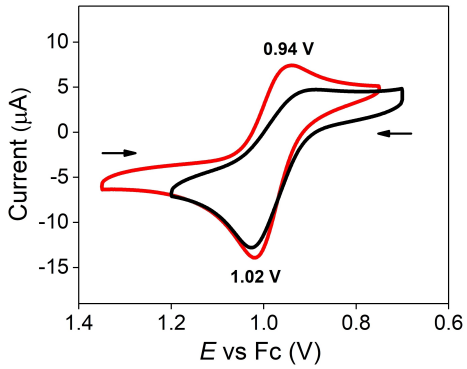

Figure 6. CV of 1 mM Co(III)–N_3 obtained in acetonitrile at room temperature (black) and −40 °C (red). Peak potentials are labeled. Other conditions: glassy carbon working electrode, Pt auxiliary electrode, Ag reference electrode, scan rate 0.1 V/s, 0.1 M KPF_6 used as electrolyte.

Co(III) to Co(IV) when performing the scan from a low starting potential. In a return scan, the corresponding cathodic peak is not observed, consistent with the low stability of **1-N$_3$** at room temperature. By contrast, when the CV is carried out at −40 °C, the redox behavior becomes quasi-reversible with an anodic and cathodic wave showing at $E_{p,a} = 1.02$ V and $E_{p,c} = 0.94$ V, respectively. Apparently, performing the measurements at a cryogenic temperature significantly increases the stability of the species generated at the anodic peak indicative of its high-valent nature. Therefore, we assign the midpoint potential of 0.98 V to the Co(IV/III) couple of **1-N$_3$**, which appears to be 0.43 V higher than that of **1-NO$_3$**.

Moreover, azide is a stronger base than nitrate in both aqueous and non-aqueous solutions and its pK_a in acetonitrile is estimated to 18.6.[13] These data lead to the estimate of the upper bound of $D(Co^{III}(N–H)N_2) = 107$ kcal/mol for complex **1-N$_3$**. Caution should be taken since this is not an accurate measurement of $D(Co^{III}(N–H)N_2)$ because the pK_a of N_3^- when bound to the cobalt center cannot be determined experimentally. Nevertheless, **1-N$_3$** has an electron affinity and a proton affinity that are both higher than those of **1-NO$_3$**. This result is in good agreement with **1-N$_3$** as a more potent oxidant than **1-NO$_3$** both thermodynamically and kinetically. In fact, **1-N$_3$** is a rare example of Co(IV) complexes capable of activating sp^3 C–H bonds stronger than 90 kcal/mol.[3b,c] The only other example is an oxoCo(IV) species that oxidizes adamantane described by Anderson and co-workers.[3a]

Moreover, it is notable that the coordination of more basic azide ligands increases the Co(IV/III) redox potential, which seems counter-intuitive because a stronger metal–ligand interaction would normally stabilize the higher-valent state. We notice in our calculations that the conversion between **1-NO$_3$** and Co(III)–NO_3 involves the removal or deposit of one electron on the Co $3d_{z2}$ orbital; however, related transformations between **1-N$_3$** and Co(III)–N_3 involve not only the transfer of an electron but also an energy crossing of the Co $3d_{z2}$ and $3d_{yz}$ MOs (Figure S15), potentially requiring a reorganization of the d-electrons. We speculate that such a complexity could cause an additional barrier for oxidizing Co(III)–N_3 and contribute to the high Co(IV/III) potential for **1-N$_3$**. Our ongoing efforts aim to use additional computational approaches to investigate these

© 2024 Wiley-VCH GmbH

15213765, 2024, 35, Downloaded from https://chemistry-europe.onlinelibrary.wiley.com/doi/10.1002/chem.202401218 by University Of Kansas, Wiley Online Library on [22/07/2024]. See the Terms and Conditions (https://onlinelibrary.wiley.com/terms-and-conditions) on Wiley Online Library for rules of use; OA articles are governed by the applicable Creative Commons License

processes in order to better understand the relationship between the Co electronic structures and the HAT reaction mechanism.

Conclusions

To summarize, in this work, we have generated a new Co(IV)–diazide complex **1-N_3** from its parent Co(IV)–dinitrate complex **1-NO_3** and employed a combination of spectroscopic and computational approaches to characterize this novel Co(IV) species. **1-N_3** is a distorted square pyramidal complex having a much shorter axial Co–N_3 bond compared to the corresponding Co–ONO_2 bond in **1-NO_3**. This greatly enhanced ligand–metal interaction in turn significantly perturbs the Co electronic structure by changing the SOMO from $3d_{z2}$ for **1-NO_3** to $3d_{yz}$ for **1-N_3** and the spectroscopic properties of the Co(IV) center (UV-vis and EPR). Furthermore, we have studied the activation of substrate C–H and O–H bonds by **1-N_3** and **1-NO_3**, showing that both complexes oxidize these two types of substrates via a HAT mechanism. **1-N_3** is a thermodynamically more potent oxidant and kinetically about one order of magnitude more reactive than **1-NO_3**. The measurements of the Co(IV/III) redox potentials for both complexes further reveal that **1-N_3** is about 0.43 V more oxidizing than **1-NO_3**. Together with azide being a stronger base than nitrate, **1-N_3** appears to have an electron affinity and a proton affinity that are both higher than those of **1-NO_3**, leading to a higher driving force for substrate oxidations. Our ongoing efforts aim to systematically modify the ligand X in a series of Co(IV)–X_2 complexes and study their effects on the substrate oxidation reactivities of resulting Co(IV) species.

In nature, high-valent Fe(IV)=O species are considered "holy grail" oxidants for substrate C–H bond activation at least in part because of the high basicity of the oxo motif.[14] While it still remains to be discovered if other non-oxo proton accepting ligands can be employed by high-valent metals in metalloenzymes that activate C–H bonds, this study suggests that high-valent M(IV) species with non-oxo ligands can certainly play or may have already played a role in related enzymatic reactions. These metal-non-oxo ligand arrays may even offer a larger degree of tunability in their oxidizing powers than the classical Fe(IV)=O species. Our work has thus broadened the scope for designing more reactive bio-inspired high-valent late transition metal complexes for activating inert aliphatic hydrocarbons.

Acknowledgements

Support of this work for M.K., Y.M.K. and D.W. was provided by the National Science Foundation (grant CHE-2102339). T.A.J., Y.L., and P.S.M. acknowledge support by the National Science Foundation (grant CHE-2154955). The calculations were performed at the University of Kansas Center for Research Computing (CRC) using the BigJay cluster resource funded through U.S. NSF grant MRI-2117449.

Conflict of Interests

The authors declare no conflict of interest.

Data Availability Statement

The data that support the findings of this study are available in the supplementary material of this article.

Keywords: High-valent cobalt(IV) · Non-oxo complex · HAT reaction · Proton accepting ligand · Redox potential

[1] a) X. Huang, J. T. Groves, *J. Biol. Inorg. Chem.* **2017**, *22*, 185–207; b) A. J. Jasniewski, L. Que Jr., *Chem. Rev.* **2018**, *118*, 2554–2592.
[2] a) D. B. Rice, A. A. Massie, T. A. Jackson, *Acc. Chem. Res.* **2017**, *50*, 2706–2717; b) P. Singh, Y. Lee, J. R. Mayfield, R. Singh, M. C. Denler, S. D. Jones, V. W. Day, E. Nordlander, T. A. Jackson, *Inorg. Chem.* **2023**, *62*, 18357–18374.
[3] a) M. K. Goetz, J. E. Schneider, A. S. Filatov, K. A. Jesse, J. S. Anderson, *J. Am. Chem. Soc.* **2021**, *143*, 20849–20862; b) J. Yang, H. T. Dong, M. S. Seo, V. A. Larson, Y.-M. Lee, J. Shearer, N. Lehnert, W. Nam, *J. Am. Chem. Soc.* **2021**, *143*, 16943–16959; c) B. Wang, Y.-M. Lee, W.-Y. Tcho, S. Tussupbayev, S.-T. Kim, Y. Kim, M. S. Seo, K.-B. Cho, Y. Dede, B. C. Keegan, T. Ogura, S. H. Kim, T. Ohta, M.-H. Baik, K. Ray, J. Shearer, W. Nam, *Nat. Commun.* **2017**, *8*, 14839; d) Y. M. Kwon, Y. Lee, A. K. Schmautz, T. A. Jackson, D. Wang, *J. Am. Chem. Soc.* **2022**, *144*, 12072–12080; e) Y. M. Kwon, Y. Lee, G. E. Evenson, T. A. Jackson, D. Wang, *J. Am. Chem. Soc.* **2020**, *142*, 13435–13441.
[4] a) J. R. Winkler, H. B. Gray, *Struct. Bond.* **2012**, *142*, 17–28; b) C. J. Ballhausen, H. B. Gray, *Inorg. Chem.* **1962**, *1*, 111–122.
[5] a) P. Mondal, M. Lovisari, B. Twamley, A. R. McDonald, *Angew. Chem. Int. Ed.* **2020**, *59*, 13044–13050; b) D. Unjaroen, R. Gericke, M. Lovisari, D. Nelis, P. Mondal, P. Pirovano, B. Twamley, E. R. Farquhar, A. R. McDonald, *Inorg. Chem.* **2019**, *58*, 16838–16848; c) P. Pirovano, A. R. McDonald, *Eur. J. Inorg. Chem.* **2018**, 547–560; d) J. K. Bower, M. S. Reese, I. M. Mazin, L. M. Zarnitsa, A. D. Cypcar, C. E. Moore, A. Y. Sokolov, S. Zhang, *Chem. Sci.* **2023**, *14*, 1301–1307; e) J. K. Bower, A. D. Cypcar, B. Henriquez, S. C. E. Stieber, S. Zhang, *J. Am. Chem. Soc.* **2020**, *142*, 8514–8521.
[6] a) S. Fukuzumi, H. Kotani, T. Suenobu, S. Hong, Y.-M. Lee, W. Nam, *Chem. Eur. J.* **2010**, *16*, 354–361; b) Y. Kang, H. Chen, Y. J. Jeong, W. Lai, E. H. Bae, S. Shaik, W. Nam, *Chem. Eur. J.* **2009**, *15*, 10039–10046; c) C. V. Sastri, J. Lee, K. Oh, Y. J. Lee, J. Lee, T. A. Jackson, K. Ray, H. Hirao, W. Shin, J. A. Halfen, J. Kim, L. Que Jr., S. Shaik, W. Nam, *Proc. Natl. Acad. Sci. USA* **2007**, *104*, 19181–19186; d) H. M. Neu, T. Yang, R. A. Baglia, T. H. Yosca, M. T. Green, M. G. Quesne, S. P. de Visser, D. P. Goldberg, *J. Am. Chem. Soc.* **2014**, *136*, 13845–13852; e) K. A. Prokop, S. P. de Visser, D. P. Goldberg, *Angew. Chem. Int. Ed.* **2010**, *49*, 5091–5095; f) A. Takahashi, D. Yamaki, K. Ikemura, T. Kurahashi, T. Ogura, M. Hada, H. Fujii, *Inorg. Chem.* **2012**, *51*, 7296–7305; g) G. Xue, C. Geng, S. Ye, A. T. Fiedler, F. Neese, L. Que Jr., *Inorg. Chem.* **2013**, *52*, 3976–3984; h) G. Xue, R. D. Hont, E. Münck, L. Que Jr., *Nat. Chem.* **2010**, *2*, 400–405; i) Y. Li, S. Handunnetthige, J. Xiong, Y. Guo, M. R. Talipov, D. Wang, *J. Am. Chem. Soc.* **2020**, *142*, 21670–21678.
[7] a) S. S. Massouda, F. A. Mautnerb, M. Abu-Youssefb, N. M. Shuaib, *Polyhedron* **1999**, *18*, 2287–2291; b) C. T. Gutman, I. A. Guzei, T. C. Brunold, *Inorg. Chem.* **2013**, *52*, 8909–8918; c) L. E. Grove, J. K. Hallman, J. P. Emerson, J. A. Halfen, T. C. Brunold, *Inorg. Chem.* **2008**, *47*, 5762–5774.
[8] a) S. Hong, F. F. Pfaff, E. Kwon, Y. Wang, M.-S. Seo, E. Bill, K. Ray, W. Nam, *Angew. Chem. Int. Ed.* **2017**, *56*, 10630–10630; b) S. Hong, F. F. Pfaff, E. Kwon, Y. Wang, M.-S. Seo, E. Bill, K. Ray, W. Nam, *Angew. Chem. Int. Ed.* **2014**, *53*, 10403–10407; c) G. B. Carpenter, G. S. Clark, A. L. Rieger, P. H. Rieger, D. A. Sweigart, *J. Chem. Soc. Dalton Trans.* **1994**, *20*, 2903–2910; d) C. V. Wilson, D. Kim, A. Sharma, R. X. Hooper, R. Poli, B. M. Hoffman, P. L. Holland, *J. Am. Chem. Soc.* **2022**, *144*, 10361–10367; e) W. Mao, D. Fehn, F. W. Heinemann, A. Scheurer, D. Munz, K. Meyer, *Angew. Chem. Int. Ed.* **2021**, *60*, 16480–16486.
[9] J. W. Darcy, B. Koronkiewicz, G. A. Parada, J. M. Mayer, *Acc. Chem. Res.* **2018**, *51*, 2391–2399.

© 2024 Wiley-VCH GmbH

15213765, 2024, 35, Downloaded from https://chemistry-europe.onlinelibrary.wiley.com/doi/10.1002/chem.202401218 by University Of Kansas, Wiley Online Library on [22/07/2024]. See the Terms and Conditions (https://onlinelibrary.wiley.com/terms-and-conditions) on Wiley Online Library for rules of use; OA articles are governed by the applicable Creative Commons License

[10] a) P. Mondal, P. Pirovano, A. Das, E. R. Farquhar, A. R. McDonald, *J. Am. Chem. Soc.* **2018**, *140*, 1834–1841; b) I. Garcia-Bosch, R. E. Cowley, D. E. Díaz, R. L. Peterson, E. I. Solomon, K. D. Karlin, *J. Am. Chem. Soc.* **2017**, *139*, 3186–3195.
[11] R. G. Agarwal, S. C. Coste, B. D. Groff, A. M. Heuer, H. Noh, G. A. Parada, C. F. Wise, E. M. Nichols, J. J. Warren, J. M. Mayer, *Chem. Rev.* **2022**, *122*, 1–49.
[12] J. T. Muckerman, J. H. Skone, M. Ning, Y. Wasada-Tsutsui, *Biochim. Biophys. Acta* **2013**, *1827*, 882–891.
[13] A. Kütt, S. Tshepelevitsh, J. Saame, M. Lõkov, I. Kaljurand, S. Selberg, I. Leito, *Eur. J. Org. Chem.* **2021**, 1407–1419.
[14] M. T. Green, J. H. Dawson, H. B. Gray, *Science* **2004**, *304*, 1653–1656.

Manuscript received: April 17, 2024
Accepted manuscript online: April 21, 2024
Version of record online: May 22, 2024

© 2024 Wiley-VCH GmbH

15213765, 2024, 35, Downloaded from https://chemistry-europe.onlinelibrary.wiley.com/doi/10.1002/chem.202401218 by University Of Kansas, Wiley Online Library on [22/07/2024]. See the Terms and Conditions (https://onlinelibrary.wiley.com/terms-and-conditions) on Wiley Online Library for rules of use; OA articles are governed by the applicable Creative Commons License